Revisiting crossflow-based stabilization in channel flows

Muhammad Abdullah and George I. Park*
Department of Mechanical Engineering & Applied Mechanics, University of Pennsylvania, Philadelphia, Pennsylvania 19104, USA

(Received 22 April 2024; accepted 1 October 2024; published 18 November 2024)

Stabilization schemes in wall-bounded flows often invoke fluid transpiration through porous boundaries. While these have been extensively validated for external flows, their efficacy in channels, particularly from the standpoint of nonmodal perturbations, is yet to be demonstrated. Here, we show that crossflow strengths previously considered "ideal" for optimizing stability in channels in fact admit strong nonmodal energy amplification. We begin by supplementing existing modal calculations and then show via the resolvent that extremely strong and potentially unfeasible crossflows are required to suppress nonmodal growth in linearly stable regimes. Investigation of unforced algebraic growth paints a similar picture. Here, a componentwise budget analysis reveals that energy redistribution through pressure-velocity correlations plays an important role in driving energy growth/decay. The superposition of a moving wall is also considered, and it is shown that while energy amplification generally worsens, it can potentially be suppressed in certain regions of parameter space. However, these flows are marred by rapidly declining mass transport, rendering their ultimate utility questionable. Our results suggest that crossflow-based stabilization might not be useful in internal flows.

DOI: 10.1103/PhysRevFluids.9.113901

I. INTRODUCTION

The control of fluid flows in channels is among the most complex open problems in classical theory, a precise understanding of which is yet to be established despite multiple decades of research. The shift from a benign laminar state to the complex chaos of turbulence is, to all appearances, highly nonlinear, and it incurs key structural and mechanistic changes in the processes driving mass and momentum transport. These modifications, depending on the exact setting, can be both desirable or undesirable, so that strategies to suppress—or even instigate—them are typically of significant interest. In this work, our aim is to reassess the efficacy of one such scheme: the superposition of a homogeneous, vertical (i.e., in the wall-normal direction) crossflow, such as that generated by a steady, spatially uniform transpiration of fluid through a porous boundary (or boundaries). Such systems have widespread utility, for example, in filtration processes, medical apparatus, and various geophysical and astrophysical phenomena, although, surprisingly, it is applications in external flows that are more frequently cited in the literature (e.g., modulating flow separation or delaying inflectional instabilities over swept wings; see Ref. [1] or Ref. [2]).

To preface with a broader perspective, the debate on transition and instability in fluid flows has undoubtedly been a long-standing one. Here, the standard analysis proceeds by deriving an eigenvalue problem from the equations of motion linearized around some base state of interest, usually laminar. Eigenmodes with positive growth rates suffer exponential amplification in time, and a critical value, Re_c, of the Reynolds number defines the threshold below which such an

*Contact author: gipark@seas.upenn.edu

instability cannot survive. For simple parabolic profiles, such as those encountered in rectilinear pressure-driven flows, this approach predicts $\mathrm{Re}_c \approx 5772$, with the Reynolds number defined based on the channel half-height h and the center-line velocity U_p. As expected, the inclusion of crossflow, described by its own Reynolds number, say R_v, dramatically alters the picture, and the first few treatments may perhaps be attributed to Refs. [3,4]. Both authors resolved, at least for small to moderate R_v, a significant increase in Re_c (again based on U_p), suggesting that the overarching influence of a net throughflow was very much stabilizing. Evidently, this remained the prevailing opinion until Ref. [5] proposed an alternative nondimensionalization of the dynamical variables, setting the streamwise maximum as opposed to U_p as the reference velocity unit. Because the injected wall-normal flux dampens the base streamwise component, this framework, they argued, preserved the distinction between the base velocity magnitude and the base velocity distribution when investigating stability. With this scaling, Ref. [5] demonstrated pockets of stabilization and destabilization, called "branches" in their terminology. To recount their example of choice, the wave number $\alpha = 1$ at $\mathrm{Re} = 6000$, known to exhibit a positive growth rate for Poiseuille flow, becomes increasingly stable until a turning point of $R_v \approx 3.4$. Thereafter, the trend reverses and the instability is restored for $R_v \gtrapprox 42.5$, only to be suppressed once again for $R_v \approx \mathcal{O}(10^2)$.

Apart from the initial study by Ref. [3], the work of Ref. [6] appears to be the first to provide a rigorous extension to the case of moving (upper) boundaries, the so-called Couette-Poiseuille flows, which present interesting stability characteristics in and of themselves. In particular, adopting the dimensionless ratio $\xi = U_c/U_p$ (the equivalent proxy in Ref. [6] is k), where U_c is the wall speed, Ref. [7] showed that complete linear stability—$\mathrm{Re}_c \to \infty$—could be achieved for $\xi \gtrapprox 0.7$, termed the "cutoff." This is, of course, not surprising since the Couette flow itself is known to be linearly stable to infinitesimal perturbations for various rheological models; see, for example, Ref. [8]. At any rate, in the presence of crossflow, Ref. [6] reported trends largely similar to the $\xi = 0$ case, except that the cutoff threshold could now be reduced to, say, $\xi \approx 0.2$ using intermediate R_v (a claim that, as they noted, was only valid for $\mathrm{Re} \leqslant 10^6$, the upper limit of their numerical study). As special instances of this base flow, "generalized" Couette-like profiles have also been investigated by Ref. [9]; these are precisely linear and develop when the influence of the crossflow in the streamwise momentum budget is neutralized by a suitably chosen pressure gradient. In the presence of viscosity, these profiles exhibit complete linear stability up to $R_v \approx 24$, beyond which the critical Reynolds number can descend to as low as the relatively mild $\mathrm{Re}_c \approx 725$ [9]. Even in the inviscid (Rayleigh) limit, excellently treated by Ref. [10], a perturbation has the potential to grow. Finally, we remark that the spatially developing (i.e., in the streamwise direction) analog has also been of interest and has been rigorously explored using Berman-type similarity solutions in the works of Refs. [11,12].

Consequently, channel flows demonstrate rich stability portraits in the presence of crossflow and form an interesting testbed for studying transition and disturbance amplification. From a purely application-oriented point of view, previous work, particularly on spatially nondeveloping cases, can be summarized in the statement by Ref. [6], who posited that modest wall velocities ξ coupled with weak-to-moderate crossflows strike the optimal balance between stability and practicality. We argue here—and this is our main contribution—that this is not necessarily the case. In particular, we cite the nonnormality of the linearized operator, typical of inertia-dominated flows, as the main culprit. Since the unstable eigenvalues are only really relevant at sufficiently large time horizons, when all other modal contributions have more or less decayed, one can rarely accurately judge the stability of a system from its spectrum alone. In shear flows, nonmodal growth mechanisms are generally more dominant and therefore more informative, which is a well-established result in hydrodynamic stability theory [13–16]. Surprisingly, despite their apparent simplicity, a comprehensive analysis on nonmodal perturbations in internal flows with crossflow is yet to be performed, at least to the best of our knowledge. One relevant work in this regard seems to be that of Ref. [17], which investigated transient, unforced energy amplification using the base flow of Ref. [5]. However, the scope of their study was rather narrow, and, as we discuss below, leaves much room for further investigation. On the other hand, the single-plate, zero-pressure-gradient analog—the so-called asymptotic suction

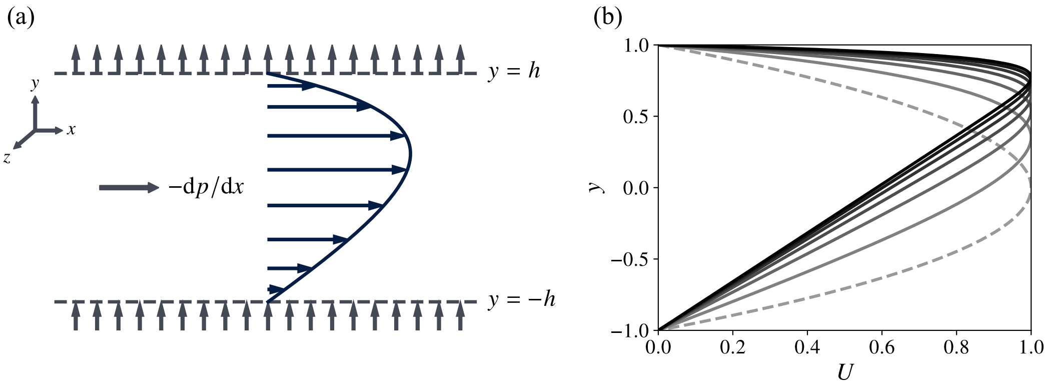

FIG. 1. (a) Diagram of the present flow geometry. (b) Streamwise velocity profiles for $R_v = 0$ (dashed line) to $R_v = 15$ in increments of 2.5. Lighter to darker shades represent increasing R_v. Note that, contrary to the convention adopted by Ref. [5], the direction of the crossflow here is from bottom to top.

boundary layer (ASBL)—has received much more attention [18–20], and we make comparisons where appropriate.

We structure this paper as follows. Section II introduces the base flow and describes our analysis frameworks. Section III augments previous discussion on eigenvalues, while Sec. IV presents a systematic summary of our nonmodal calculations, with a particular focus on the purely pressure-driven case. Section V investigates the effects of wall motion, and Sec. VI presents conclusions.

II. PROBLEM FORMULATION

A. Base flow

We begin our analysis with the standard Navier-Stokes equations. In dimensional terms, these read

$$\frac{D\boldsymbol{u}}{Dt} = \frac{1}{\rho}(\nabla \cdot \mathsf{T}), \tag{1}$$

$$\nabla \cdot \boldsymbol{u} = 0, \tag{2}$$

where $D/Dt \equiv \partial/\partial t + (\boldsymbol{u} \cdot \nabla)$ is the total derivative, $\mathsf{T} = -p\mathsf{I} + 2\mu\mathsf{e}$ is the Cauchy stress, and $\mathsf{e} = [\nabla\boldsymbol{u} + (\nabla\boldsymbol{u})^{\mathsf{T}}]/2$ is the symmetric rate-of-strain tensor. Here, Eq. (2) encodes the usual incompressibility constraint. The system of interest in this study can be summarized in the schematic presented in Fig. 1(a). An incompressible Newtonian fluid, confined between two rigid, porous, infinite boundaries positioned at $y = \pm h$, is driven by a constant streamwise pressure gradient $-dp/dx > 0$. A vertical crossflow is imposed by introducing a uniform injection, V_i, and suction, V_s, of fluid through the lower and upper walls, respectively. We assume a fully developed flow, so that $\partial/\partial x = \partial/\partial z \equiv 0$ and the compatibility of the boundary conditions with the continuity equation demands $V_i = V_s = V_0$.

As noted earlier, the sensible selection of a reference velocity for this system is rather nuanced. The usual (and admittedly immediate) choice is U_p, the center-line velocity for the Poiseuille flow in the absence of crossflow. However, the streamwise velocity is directly coupled to—and decreases—with the crossflow strength, requiring an increasing pressure differential to maintain the same maximum [5]. Thus, for sufficiently large V_0, U_p is no longer a physically meaningful metric. Consequently, we adopt U_m, the streamwise maximum, as our characteristic velocity. With the channel half-width h as our length scale, the associated Reynolds number becomes $\mathrm{Re} = U_m h/\nu$, where ν is the kinematic viscosity, and the dimensionless form of the governing equations can be written as

$$\boldsymbol{u}_t + (\boldsymbol{u} \cdot \nabla)\boldsymbol{u} = -\nabla p + \frac{1}{\mathrm{Re}}\nabla^2 \boldsymbol{u}, \tag{3}$$

$$\nabla \cdot \boldsymbol{u} = 0. \tag{4}$$

Furthermore, with the crossflow Reynolds number $R_v = V_0 h/\nu$, the stationary laminar profile becomes

$$\boldsymbol{U} = (U(y, R_v),\ \ V_0/U_m,\ \ 0)^\intercal = (U(y, R_v),\ \ R_v/\,\mathrm{Re},\ \ 0)^\intercal, \tag{5}$$

where

$$U(y, R_v) = \frac{R_v(y - \operatorname{csch} R_v e^{R_v y} + \coth\ R_v)}{R_v \coth\ R_v - 1 - \log\,(R_v \operatorname{csch} R_v)}. \tag{6}$$

Figure 1(b) illustrates U plotted against the nondimensional y coordinate for some representative values of R_v. Since the (nondimensional) streamwise maximum has been fixed to unity, the primary effect of a stronger crossflow is to skew the profile in the positive wall-normal direction. Consequently, as noted by Ref. [5], a very thin boundary layer develops near the upper (suction) wall, leaving an approximately linear profile throughout the remainder of the channel. In fact, one can show that

$$\lim_{R_v \to \infty} U(y, R_v) = \tfrac{1}{2}(1 + y) \tag{7}$$

in the channel bulk, which, save for the different top-wall boundary condition, is precisely the well-known Couette profile for viscous flow between two parallel surfaces in relative motion. Thus, as $R_v \to \infty$, complete linear stability may be expected. On the other hand, the absence of crossflow, $R_v = 0$, yields the Poiseuille flow, although establishing this directly from Eq. (6) requires additional care, since $U(y, R_v)$ is not defined in this limit. In fact, $R_v = 0$ is a removable singularity for U, and the appropriate power expansion

$$U(y, R_v) = (1 - y^2) + \frac{R_v}{3}(y - y^3) + O\big(R_v^2\big) \tag{8}$$

informs the smooth continuation of $U(y, R_v)$ over all $R_v \in \mathbb{R}$.

B. Linearized equations

To formulate the stability problem, we rewrite the Navier-Stokes equations in operator format,

$$\frac{\partial \boldsymbol{\chi}}{\partial t} = g(\boldsymbol{\chi}), \tag{9}$$

where $\boldsymbol{\chi}$ is the state vector and g is a nonlinear differential operator. Representing the base profile as $\overline{\boldsymbol{\chi}}$, we consider a set of infinitesimal fluctuations $\boldsymbol{\chi}'$ and perform a Jacobian linearization of g around $\overline{\boldsymbol{\chi}}$. The result is a system of linearized evolution equations for $\boldsymbol{\chi}'$, which, in the traditional fourth-order formulation involving perturbations around the wall-normal velocity/vorticity (v', η'), reads

$$\left[\left(\frac{\partial}{\partial t} + U\frac{\partial}{\partial x} + V\frac{\partial}{\partial y}\right)\nabla^2 - \frac{d^2U}{dy^2}\frac{\partial}{\partial x} - \frac{1}{\mathrm{Re}}\nabla^4\right]v' = 0, \tag{10}$$

$$\left[\frac{\partial}{\partial t} + U\frac{\partial}{\partial x} + V\frac{\partial}{\partial y} - \frac{1}{\mathrm{Re}}\nabla^2\right]\eta' + \frac{dU}{dy}\frac{\partial v'}{\partial z} = 0. \tag{11}$$

Here, $\nabla^4\langle\cdot\rangle = \nabla^2(\nabla^2\langle\cdot\rangle)$ is the standard biharmonic operator acting in Cartesian space, and U and V are the streamwise and wall-normal components of the background flow, Eq. (5). The appropriate boundary conditions follow from the no-slip and impermeability restrictions at the wall

$$v'|_{y=\pm 1} = \eta'|_{y=\pm 1} = \partial v'/\partial y|_{y=\pm 1} = 0. \tag{12}$$

In what follows, the prime notation is dropped with the understanding that all discussion is based on the disturbance field, unless explicitly noted. We exploit the spatial homogeneity in the wall-parallel directions by applying a wavelike ansatz

$$(v, \eta) = (\widetilde{v}(y, t), \widetilde{\eta}(y, t))e^{i(\alpha x+\beta z)} + \text{c.c.}, \tag{13}$$

where $\alpha, \beta \in \mathbb{R}$ represent the spatial wave numbers. The result is the Orr-Sommerfeld-Squire initial-value problem:

$$\mathsf{L}\boldsymbol{q} = -\frac{\partial}{\partial t}\mathsf{M}\boldsymbol{q} \Rightarrow \frac{\partial \boldsymbol{q}}{\partial t} = (-\mathsf{M}^{-1}\mathsf{L})\boldsymbol{q} \Rightarrow \frac{\partial \boldsymbol{q}}{\partial t} = \mathsf{S}'\boldsymbol{q}. \tag{14}$$

In Eq. (14), $\boldsymbol{q} = (\widetilde{v} \quad \widetilde{\eta})^{\mathsf{T}}$ and, by denoting $\mathsf{D} \equiv \partial/\partial y$ and $k^2 = \alpha^2 + \beta^2$, the block operators L and M are

$$\mathsf{L} = \begin{pmatrix} \mathsf{L}_{\mathrm{OS}} & 0 \\ i\beta \mathsf{D}U & \mathsf{L}_{\mathrm{SQ}} \end{pmatrix}, \quad \mathsf{M} = \begin{pmatrix} \mathsf{D}^2 - k^2 & 0 \\ 0 & 1 \end{pmatrix}, \tag{15}$$

where

$$\mathsf{L}_{\mathrm{OS}} = (i\alpha U + V\mathsf{D})(\mathsf{D}^2 - k^2) - i\alpha \mathsf{D}^2 U - \frac{1}{\mathrm{Re}}(\mathsf{D}^2 - k^2)^2, \tag{16}$$

$$\mathsf{L}_{\mathrm{SQ}} = i\alpha U + V\mathsf{D} - \frac{1}{\mathrm{Re}}(\mathsf{D}^2 - k^2). \tag{17}$$

The condition for Hurwitz stability can then be written as $\Re(\lambda) < 0$ for all $\lambda \in \Lambda(\mathsf{S}')$, where $\Lambda(\mathsf{S}')$ denotes the spectrum of S'. Typically, these eigenvalues are subsequently related to a set of complex circular frequencies $\omega = \omega_r + i\omega_i$, such that $\lambda = -i\omega$, rephrasing the stability constraint as $\omega_i < 0$ [21]. This completes the definition of the normal mode in Eq. (13), that is,

$$(v, \eta) = (\widetilde{v}(y, t), \widetilde{\eta}(y, t))e^{i(\alpha x+\beta z)} = (\hat{v}(y), \hat{\eta}(y))e^{i(\alpha x+\beta z-\omega t)}. \tag{18}$$

In this approach, we are particularly interested in the manifold of neutral stability, defined here by the locus

$$\omega_i(\alpha, \beta, \mathrm{Re}, R_v) = 0. \tag{19}$$

It is well-known, however, that a naive analysis of the spectral abscissa in this way is often very limiting, especially in shear flows, because it provides predictions of flow stability only at asymptotically long times. In contrast, significant energy growth can be initiated by nonmodal mechanisms operating on much shorter time scales, potentially violating the linear assumption prior to the emergence of the unstable eigenmode, if any, and encouraging the onset of nonlinear interactions (possibly even turbulence). A model for this behavior lies in the nonnormality of S', whose commutator with its adjoint $\mathsf{S}'^{\dagger}$ need not vanish:

$$[\mathsf{S}', \mathsf{S}'^{\dagger}] = \mathsf{S}'\mathsf{S}'^{\dagger} - \mathsf{S}'^{\dagger}\mathsf{S}' \neq 0. \tag{20}$$

As a corollary, S' admits oblique (nonorthogonal) eigenfunctions that, in a basis expansion, can allow for finite-time energy growth, evidently in both sub- and supercritical parameter regimes. This (purely linear) mechanism is often identified as a likely motivator for the so-called *bypass* route to transition [16,22], and has even found utility in elucidating key physical mechanisms driving fully turbulent flows; see, for example, Refs. [23–25].

To explore the potential for nonmodal growth here, we work from the most general case, that is, when the initial-value problem in Eq. (14) is driven by a time-harmonic forcing $\mathsf{F}(y, t) = \mathsf{f}(y)e^{-i\nu t}$.

Thus, we write

$$\frac{\partial \boldsymbol{q}}{\partial t} = -i\mathsf{S}\boldsymbol{q} + \mathsf{F} \Rightarrow \frac{\partial \boldsymbol{q}}{\partial t} = -i\mathsf{S}\boldsymbol{q} + \mathsf{f}(y)e^{-i\upsilon t}, \tag{21}$$

where $\upsilon \in \mathbb{C}$ and $\mathsf{S} = i\mathsf{S}'$. Since S' is time-independent, the system response is

$$\boldsymbol{q}(t) = \Phi(t)\boldsymbol{q}(0) + \int_0^t \Phi(t - \mathsf{t})\mathsf{F}(y, \mathsf{t})\, d\mathsf{t}, \tag{22}$$

where $\Phi(t) \equiv e^{-i\mathsf{S}t}$ is the solution propagator, which maps the initial state of the system $\boldsymbol{q}_0$ at $t' = 0$ to its value at $t' = t$. Consider now the special case where $\mathsf{F} = 0$; under appropriate norms in the input and output spaces, the gain can be defined as

$$G(\alpha, \beta, \mathrm{Re}, R_v, t) = \sup_{q_0 \neq 0} \frac{\|\boldsymbol{q}\|_{\mathrm{out}}^2}{\|\boldsymbol{q}_0\|_{\mathrm{in}}^2}, \tag{23}$$

and represents, at time t, the largest energy growth optimized over all possible initial conditions having unit norm [15]. As a physically meaningful metric, the energy norm is adopted here (see, for example, Ref. [22]), so that $\|\cdot\|_{\mathrm{in}} = \|\cdot\|_{\mathrm{out}} = \|\cdot\|_E$ and

$$\|\boldsymbol{q}\|_E^2 = \int_{-1}^{1} \widetilde{v}^*\widetilde{v} + \frac{1}{k^2}(\widetilde{\eta}^*\widetilde{\eta} + \mathsf{D}\widetilde{v}^*\mathsf{D}\widetilde{v})\, dy. \tag{24}$$

It follows that $G = \|\Phi(t)\|_E^2$. Hereafter, there are two equally valid approaches: (i) project onto the space of eigenfunctions using the Gramian matrix [15,26], or (ii) employ a similarity transformation incorporating information on the nonuniform grid spacing [14], which is the route we adopt here. In particular, one can write

$$\|\boldsymbol{q}\|_E^2 \simeq \boldsymbol{q}^*\mathsf{M}\boldsymbol{q}, \tag{25}$$

where

$$\mathsf{M} = \frac{1}{k^2}\begin{pmatrix} \mathsf{D}^\dagger\mathsf{W}\mathsf{D} + k^2\mathsf{W} & 0 \\ 0 & \mathsf{W} \end{pmatrix} \tag{26}$$

is Hermitian positive-definite and W is a diagonal matrix comprising the Clenshaw-Curtis quadrature weights [27]. With a Cholesky decomposition $\mathsf{M} = \mathsf{Q}^\dagger\mathsf{Q}$, we find

$$\|\boldsymbol{q}\|_E^2 \simeq \boldsymbol{q}^\dagger\mathsf{Q}^\dagger\mathsf{Q}\boldsymbol{q} = \|\mathsf{Q}\boldsymbol{q}\|_2^2, \tag{27}$$

so that

$$G = \sup_{q_0 \neq 0} \frac{\|\mathsf{Q}\Phi(t)\boldsymbol{q}_0\|_2^2}{\|\mathsf{Q}\boldsymbol{q}_0\|_2^2} = \sup_{q_0 \neq 0} \frac{\left\|\mathsf{Q}\Phi(t)\mathsf{Q}^{-1}\mathsf{Q}\boldsymbol{q}_0\right\|_2^2}{\|\mathsf{Q}\boldsymbol{q}_0\|_2^2} = \left\|\mathsf{Q}\Phi(t)\mathsf{Q}^{-1}\right\|_2^2, \tag{28}$$

which can be immediately computed using a standard singular value decomposition. In this setting, the right and left singular vectors represent, respectively, the initial condition and response pair that achieve this gain at time t.

However, if $\mathsf{F} \neq 0$, then assuming asymptotic stability of S', the long-time response reduces to

$$\boldsymbol{q}(t) = -ie^{-i\upsilon t}(\mathsf{S} - \upsilon\mathsf{I})^{-1}\mathsf{f}(y). \tag{29}$$

Here, the resolvent $\mathsf{R} \equiv (\mathsf{S} - \upsilon\mathsf{I})^{-1}$ becomes the quantity of interest, encoding important information about the spectral properties of the system. In particular, if the excitation frequency is resonant, so that $\upsilon \in \Lambda(\mathsf{S})$, the resolvent is ill-defined and its norm $\|\mathsf{R}\|_E$ tends to infinity. However, for systems whose dynamics are governed by nonnormal operators, this norm may be large even when υ is merely pseudoresonant, that is, $\upsilon \notin \Lambda(\mathsf{S})$. If υ is restricted to real frequencies, then the analysis can, in a sense, be physically motivated, with the resolvent describing the perturbed linear operator resulting from, for example, exogeneous vibrations or experimental imperfections [13].

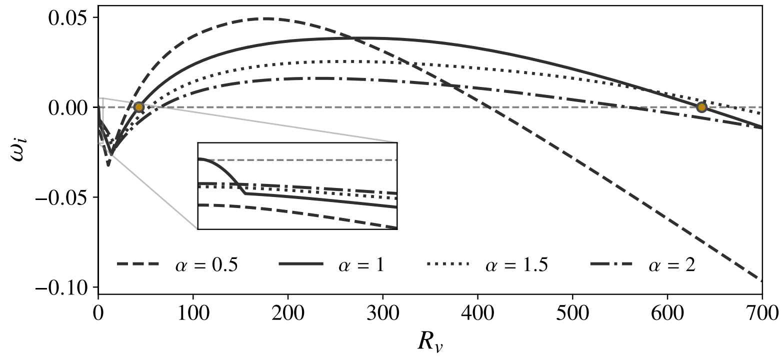

FIG. 2. At Re $= 6000$, the growth rates ω_i versus R_v for the most unstable eigenmode corresponding to $\alpha \in \{0.5, 1, 1.5, 2\}$. The gray dashed line denotes the stability boundary $\omega_i = 0$. For $\alpha = 1$, the Branch-I and Branch-II R_v have been emphasized through circles.

Generalizing to the complex plane allows for the definition of the so-called ϵ-pseudospectrum, the set of values given by

$$\Lambda_\epsilon(\mathsf{S}) = \{\upsilon \in \mathbb{C} : \|\mathsf{R}\|_E \geqslant 1/\epsilon\}. \tag{30}$$

For normal operators, the ϵ-pseudospectra, at least under an appropriate 2-norm as chosen here, correspond to closed ϵ-balls centered around the spectrum. Nonnormality, however, allows for more complicated pseudospectral boundaries, and the extent to which they protrude into the stable half of the complex plane can have important implications for energy growth in the unforced initial-value problem—see, for example, Ref. [26] or Ref. [14].

To discretize the stability operators, we implement a standard Chebyshev pseudospectral method written in `Python`. Our in-house solver has been extensively validated against classical rectilinear geometries, including the (Newtonian and Oldroyd-B) Poiseuille flow, the Couette flow, and the Couette-Poiseuille flow, and has recently been used in the linear analysis of three-dimensional boundary layers [28]. In most of the calculations presented here, unless specifically noted, we employed $N = 256$ Chebyshev modes, resulting in a $(2N + 2) \times (2N + 2)$ matrix system. We determined that this resolution was sufficient—and occasionally necessary—to achieve convergence for the values of R_v treated here. All modal and nonmodal calculations were performed in `SciPy`. To accelerate our output, we additionally scaled to an embarrassingly parallel workload using the `Python` module `Ray` [29]. Finally, the ϵ-pseudospectra were created using Eigentools [30].

III. MODAL ANALYSIS

We begin by supplementing classical perspectives on the modal stability of this flow. We define the critical Reynolds number, Re_c, as the smallest value of the Reynolds number below which the flow is linearly stable. At this threshold, a disturbance, described by the critical wave number (α_c, β_c) must achieve neutral stability. Despite a nonzero mean velocity component in the wall-normal direction, Squire's transformation [31] remains applicable, allowing us to set $\beta_c = 0$ *a priori* and restrict attention to transversal modes. Furthermore, similarly to the purely streamwise case, the Squire operator (see Eqs. (15) and (17)) can be conveniently ignored, since the associated eigenmodes are necessarily damped. Thus, only the Orr-Sommerfeld equation is of relevance when treating modal stability.

To preface the ensuing discussion, we cite a key finding from Ref. [5], referring in the process to Fig. 2, which plots at Re $= 6000$ the growth rate ω_i corresponding to the least stable eigenmode for various representative choices of the streamwise wave number α. Reference [5] focused specifically on the case $\alpha = 1$, which is unstable for the Poiseuille flow ($R_v = 0$), and showed that it experienced stabilization followed by destabilization for small to intermediate R_v; see Fig. 2. Subsequently, at

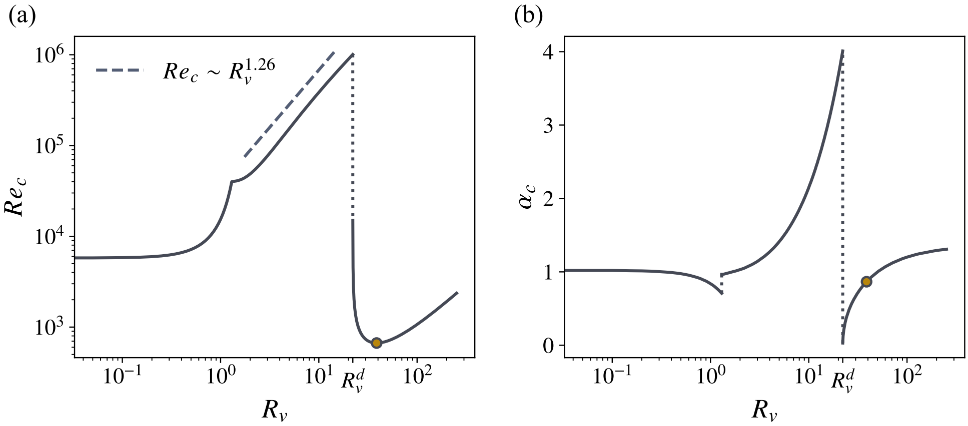

FIG. 3. Critical flow parameters versus the crossflow Reynolds number R_v: (a) the critical Reynolds number Re_c and (b) critical streamwise wave number, α_c. In each panel, the dotted lines elucidate regions of discontinuity, with $R_v = R_v^d$ being common to both Re_c and α_c. Furthermore, a circle indicates the flow parameters minimizing Re_c. Finally, in panel (a), the dashed line represents the scaling $\mathrm{Re}_c \sim R_v^{1.26}$.

the so-called "Branch-I" R_v ($\approx$42.91), exponential growth could be reestablished (cf. Ref. [5], the mode became unstable "again") and sustained until the "Branch-II" R_v ($\approx$636.16), which initiated yet another region of stability. Evidently, as verified in Fig. 2, this classification is not appropriate for all combinations of (α, Re), for example, $(\alpha, \mathrm{Re}) = (0.5, 6000)$. In fact, since the upper and lower branches of the Poiseuille neutral curve decay as $\mathrm{Re}^{-1/11}$ and $\mathrm{Re}^{-1/7}$ at large Re (see, for example, Refs. [32,33]), such a R_v cannot be demarcated for *any* Re at even smaller wavelengths, say $\alpha \geqslant 1.5$. Reference [6] recognized this and circumvented the problem by introducing a third branch, whose existence was predicated on the stability of $(\alpha, \mathrm{Re}, R_v = 0)$ and marked the transition from unstable to stable when R_v initially increases from zero. In summary, a more refined characterization was needed, and here we attempt to add to the discussion.

Figure 3 summarizes a numerical search for the critical parameters $(\alpha_c, \mathrm{Re}_c)$ for the range $0 \leqslant R_v \leqslant 250$. Similarly to previous studies, we ignore $R_v < 0$ due to the invariance of the eigenproblem under the transformation $(y, R_v) \to (-y, -R_v)$. Consistent with the narrative suggested by Fig. 2, we observe a rather sharp, monotonic increase in the critical Reynolds number Re_c through $R_v \lessapprox 1$. This trend persists beyond this interval, adjusting, however, to an approximate power-law behavior, $\mathrm{Re}_c \sim R_v^{1.26}$. Throughout the latter range, the value of Re_c increases rapidly to $\mathrm{Re}_c \approx \mathcal{O}(10^6)$, before abruptly descending to $\mathrm{Re}_c \approx \mathcal{O}(10^3)$ at $R_v = R_v^d \approx 22.175$. Shortly thereafter, the minimum of $\mathrm{Re}_c \approx 667.48730$ is achieved at the turning point $R_v \approx 38.75$, which is in good agreement with the findings of Ref. [5]. Meanwhile, the critical streamwise wave number α_c initially experiences a brief drop from its value at $R_v = 0$ ($\alpha_c \approx 1.02$), before discontinuously recovering at $R_v \approx 1$—note that such a discontinuity does not exist for Re_c. Following this, with stronger crossflows, we observe an increasing preference for short-wavelength instabilities up to the critical value of $R_v = R_v^d$. Here, in conjunction with one in Re_c, another discontinuity is encountered and α_c rapidly descends to near-zero ($\approx\mathcal{O}(10^{-2})$ with the extent of our computation) before rising to what appears to be an asymptote. We remark here that for $20.8 \lessapprox R_v \lessapprox 22$, Ref. [6] report an unconditional linear *stability* for the Poiseuille flow (in fact, even for the Couette-Poiseuille flow $\xi \neq 0$—see Sec. V), which is in contrast to Fig. 3. According to our understanding, this discrepancy appears to be due to a combination of insufficient numerical resolution (they used $N = 120$ collocation points) and a restriction of their search space to $\mathrm{Re} \leqslant 10^6$. We verified that our calculations remained robust even when the resolution was doubled, indicating genuine instability.

To unravel the discontinuous nature of the critical parameters, Fig. 4 details the movement of the neutral stability curves (NSCs) in the (α, Re) plane, particularly before and after $R_v = R_v^d$. Focusing

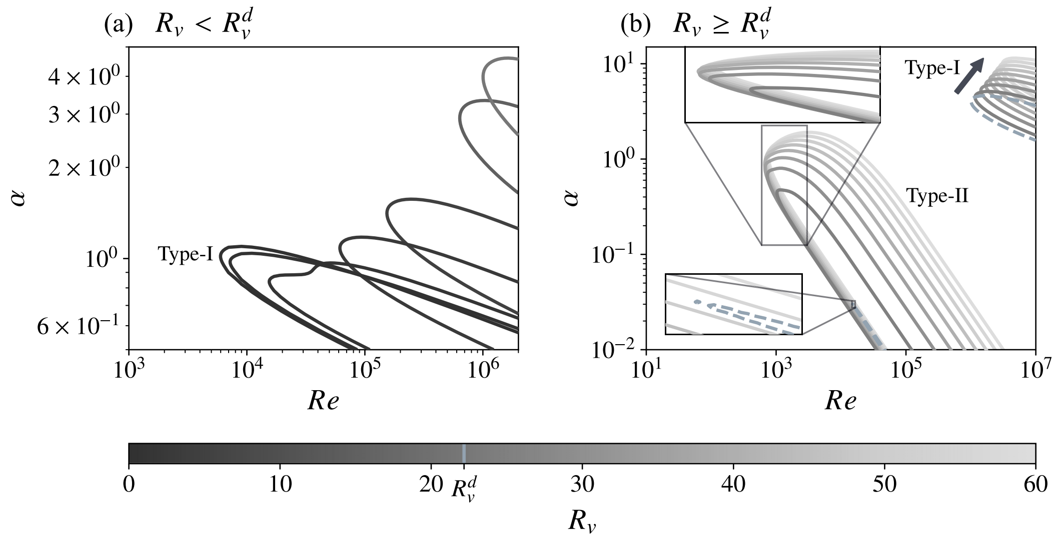

FIG. 4. Movement of the neutral curves in the (α, Re) plane for (a) $R_v < R_v^d$ and (b) $R_v \geqslant R_v^d$. Where appropriate, Type-I and Type-II instabilities have been labeled. For panel (b), specifically, an inset zooms in on the development of the Type-II NSCs; in the same panel, the dashed contours correspond to $R_v = R_v^d$.

first on $R_v < R_v^d$, Fig. 3(a) indicates that the presence of crossflow is exclusively stabilizing, and this is verified in Fig. 4(a) by a net displacement of the NSCs in the direction of increasing Re. A secondary minimum develops at intermediate R_v in this range, which quickly coalesces with the primary one and appears to signal a small jump in the NSC toward larger wave numbers, consistent with the first discontinuity for α_c observed in Fig. 3(b). Henceforth, the NSCs continue to shift deeper into the upper-right corner of the (α, Re) plane.

Beyond $R_v = R_v^d$, more dynamic behavior can be resolved. Specifically, two *different* NSCs begin to coexist. The first set of unstable modes, relegated to $\mathrm{Re} \geqslant O(10^6)$, can effectively be traced back to the (sole) NSC that occurs for $R_v < R_v^d$ and, as such, can be interpreted as its continuation into this R_v regime. Neither Ref. [5] nor Ref. [6] reported this, instead implying the presence of a single NSC for all unstable R_v; we label these (and their counterparts in $R_v < R_v^d$) as "Type-I" instabilities and note that in both R_v regimes, they generally exhibit a monotonic displacement toward increasing Re as the crossflow becomes stronger. The second group of instabilities, deemed "Type-II" and active only in $R_v \geqslant R_v^d$, manifest in the form of an NSC emerging from $\alpha \approx 0$ and are, of course, precisely those reported in previous work since they formally define criticality for this R_v regime. As highlighted in the inset of Fig. 4(b) these modes temporarily destabilize before stabilizing, defining in the process the turning point observed for Re_c in Fig. 3(a).

To dissect the physical mechanism driving the instability, one can turn to the perturbation energy budget, governed by the following balance equation [15]:

$$\frac{d\mathsf{E}}{dt} = \frac{d}{dt}\int_{-1}^{1} \frac{u_i u_i}{2}\, dy = \int_{-1}^{1} \mathsf{PR}\, dy - \int_{-1}^{1} \mathsf{VD}\, dy, \tag{31}$$

where we have adopted the Einstein notation and defined

$$\mathsf{PR} = \underbrace{-uv}_{\tau}\, \mathsf{D}U, \tag{32}$$

$$\mathsf{VD} = \frac{1}{\mathrm{Re}} \frac{\partial u_i}{\partial x_j} \frac{\partial u_i}{\partial x_j}. \tag{33}$$

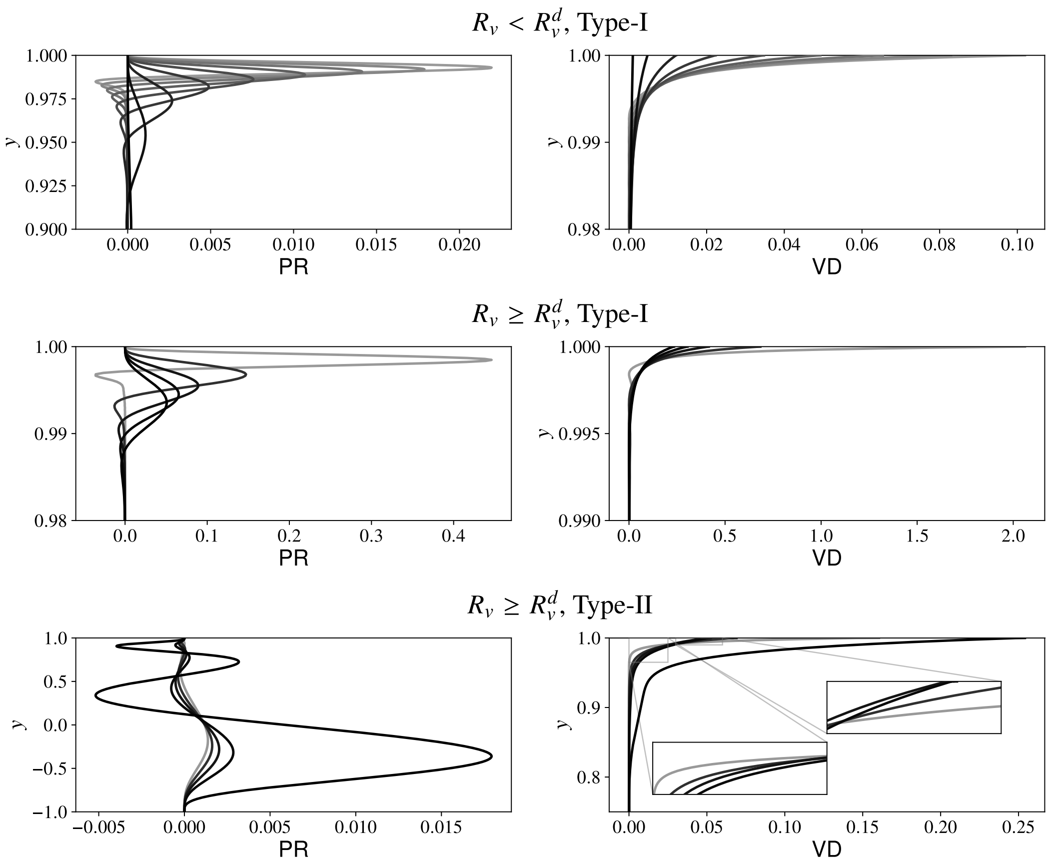

FIG. 5. Distributions of the energy production PR (left) and dissipation VD (right) for Type-I and Type-II modes at criticality. Here, for $R_v < R_v^d$, we consider $R_v \in \{0.5, 2.5, 5, 7.5, 10, 12.5, 15, 17.5, 20\}$, whereas for $R_v \geqslant R_v^d$, $R_v \in \{22.24, 26, 32, 45, 95\}$. In each panel, darker shades represent weaker crossflows.

Here, PR represents production against the background shear (contributed to only by DU) and is responsible for the transfer of energy from the base flow to the disturbance through the action of the Reynolds stress τ. The second term VD $\geqslant 0$ instead denotes viscous dissipation. In general, a (positive) production destabilizes, whereas dissipation stabilizes the disturbance field, although for a neutrally stable mode, as we will discuss here, these contributions must exactly cancel.

Figure 5 explores for Type-I and Type-II instabilities the spatial variation of terms that contribute to the energy budget at criticality. For Type-I modes below R_v^d, energy production PR operates primarily near the suction boundary, its peak becoming sharper in tandem with R_v. For the weakest crossflow strengths in this range, an additional small positive hump (not shown here) can also be resolved near the lower wall, although it decays very rapidly as R_v increases. Similarly, viscous dissipation VD remains confined to the upper wall and also increases in conjunction with PR, as required to ensure neutral growth. As highlighted in the second row of Fig. 5, these trends appear to translate well to a Type-I criticality in $R_v \geqslant R_v^d$, which provides further evidence that they are, in fact, a continuation of Type-I modes from $R_v < R_v^d$. However, for Type-II instabilities, the picture changes dramatically. Here, PR develops noticeable regions of energy negation and, more importantly, a wide positive peak in the lower (injection) half of the channel. We find the latter behavior quite intriguing, particularly in light of recent work showing that it is, in fact, the boundary inflow (outflow) that supports destabilization (stabilization); see Ref. [10]. Equally important to

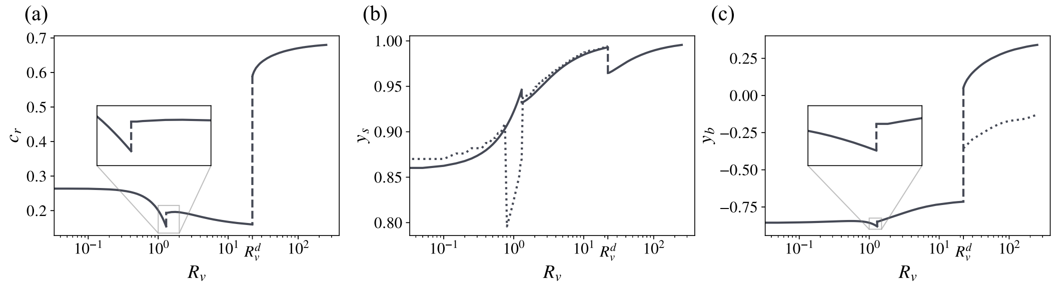

FIG. 6. Movement of the critical layers with R_v: (a) the real part of the phase speed at criticality (note that $c_i = 0$ by definition of neutral stability), (b) y_s, the critical layer near the suction (upper) wall, and (c) y_b, the critical layer near the injection (lower) wall. In panels (b) and (c), the dotted lines represent the wall-normal locations where PR is maximized.

mention here is that for moderate to large crossflows (such as those found in $R_v \geqslant R_v^d$), variations in the streamwise shear DU are primarily located near the upper wall (with D$U \to 1/2$, the Couette value, elsewhere). However, since the amplitude of positive production instead peaks specifically near the lower wall, we conclude that the crossflow influences Type-II modes predominantly through modification of the Reynolds stress (i.e., τ) distribution.

Formally, the last row in Fig. 5 corresponds to the regime explored in Sec. 5 of Ref. [6]. In their Fig. 17, for example, they reported that the dissipation at criticality for $(\xi, R_v) = (0.5, 25)$ was completely overshadowed by the energy production throughout the channel width. Therefore, any removal of energy from the perturbation field arose directly from energy negation, rendering the movement of the critical layers, as they say, "irrelevant." Clearly, as highlighted in Fig. 5, this is not an entirely robust mechanism, at least for $\xi = 0$, since, despite neutrality, VD for $R_v \geqslant R_v^d$ operates at least one order of magnitude higher than PR and generally intensifies with R_v. In other words, investigating the critical layers, the set of points where $U(y) = c_r$, could be instructive here. These points constitute regular singularities for the stability equations in the Rayleigh limit, but are smoothed over with the addition of viscosity in the Orr-Sommerfeld-Squire formulation. More importantly, it is well known that peaks in the amplitude of energy production are usually located within these layers [6,15,34,35].

Figure 6(a) presents the variation of c_r at criticality versus R_v; we immediately observe discontinuities synonymous with those of α_c, Fig. 3(b). The exact location of the associated critical layers can be explicitly determined as the solution(s) to the following transcendental equation:

$$U(y) = c_r \Rightarrow y - \operatorname{csch} R_v e^{R_v y} = \Pi_1, \tag{34}$$

where we have elected to set

$$\Pi_1 = \frac{\Pi_2 c_r}{R_v} - \coth R_v, \tag{35}$$

$$\Pi_2 = R_v \coth R_v - 1 - \log(R_v \operatorname{csch} R_v). \tag{36}$$

Equation (34) is satisfied by

$$y = \Pi_1 - \frac{1}{R_v} W_n(\Pi_3), \tag{37}$$

where W_n is the nth-branch of Lambert's W-function and $\Pi_3 = -R_v \operatorname{csch} R_v e^{\Pi_2 R_v}$. Here, since $-1/e \leqslant \Pi_3 < 0$, there exist two distinct critical layers [which can alternatively be concluded by noting that $c_r < 1$ and inspecting the velocity profiles in Fig. 1(b)], and we only need to consider $n \in \{-1, 0\}$. We observe that, as $R_v \to 0$, the symmetry of the resulting profile requires the absolute values of these roots to coalesce, despite being in opposite halves of the channel. Thus, the solutions,

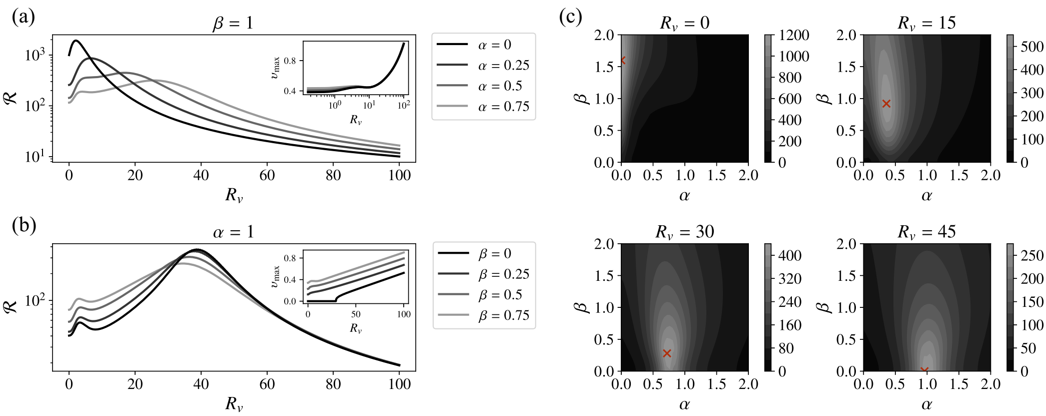

FIG. 7. For various wave number pairs at $\mathrm{Re} = 600$, plots of $\mathcal{R}$, the maximum resolvent norm over all real forcing frequencies: (a) $\beta = 1$ and α increased from $\alpha = 0$ to $\alpha = 0.75$ in increments of 0.25 and (b) $\alpha = 1$, with β varied in a similar manner. The insets show the maximizing frequency $\upsilon_{\max}$. Furthermore, panel (c) shows contours of $\mathcal{R}(\alpha, \beta)$ for various R_v; here, a red cross in each panel marks the global optimal.

which we label y_s and y_b, respectively, can be naturally identified with the suction (top) and injection (lower) boundaries. However, due to the asymmetry inflicted upon U by the crossflow, one can expect both critical layers to eventually shift toward the upper half of the channel, an intuition that is verified in Figs. 6(b) and 6(c). Specifically, commensurate with the movement of the maximum in energy production PR for Type-I modes, y_s generally increases, effectively approaching $y_s = 1$ for sufficiently large R_v. Interestingly, this trend is broken around $R_v \approx 1$, i.e., when the first discontinuity in α_c is encountered. Meanwhile, beyond $R_v = R_v^d$, y_b undergoes a sudden jump into the suction half of the channel, exhibiting in the process a weaker but still positive correlation with the location of the peak energy production for Type-II modes.

IV. NONMODAL ANALYSIS

We now direct our focus toward nonmodal energy amplification. As shown in Sec. III, an increase in the crossflow component starting from $R_v = 0$ generally has a stabilizing effect, at least in the sense of the critical Reynolds number. Following a paradigm shift at $R_v = R_v^d$, however, positive growth rates can be achieved for Reynolds numbers as low as $\mathrm{Re} \approx 650$. When operating solely on this information, one would conclude that the most optimal (and practical) stabilization is granted by weak to, at best, modest R_v. In this section, we show that nonnormality indicates an entirely different story.

We begin by inspecting the resolvent R; in particular, we define the following quantity:

$$\mathcal{R}(\alpha, \beta, \mathrm{Re}, R_v) = \max_{\upsilon \in \mathbb{R}} \|\mathsf{R}\|_E(\alpha, \beta, \mathrm{Re}, R_v, \upsilon), \tag{38}$$

which, if the resolvent is interpreted as a transfer function between the excitation and its response, represents an H_∞-norm. In Fig. 7, we visualize $\mathcal{R}$, along with the maximizing frequency $\upsilon = \upsilon_{\max}$, for some sample wave numbers at $\mathrm{Re} = 600$, which is subcritical and, therefore, admits no modal instability for all R_v treated here.

We first comment on longitudinal ($\alpha = 0$) and transverse ($\beta = 0$) perturbations. The former class typically elicits the strongest resolvent response for purely streamwise base flows. Therefore, we expect this trend to persist at least for weak R_v, and this is verified in Fig. 7(a). In fact, we see that the amplification of streamwise-independent modes can even be intensified in the presence of small amounts of crossflow. As an example, for $R_v \approx 2$, for which Fig. 3(a) predicts $\mathrm{Re}_c \approx 48\,500$, $\mathcal{R} \approx 2000$, so that a unit norm forcing can produce $\mathcal{O}(10^3)$ energy growth (compare this with

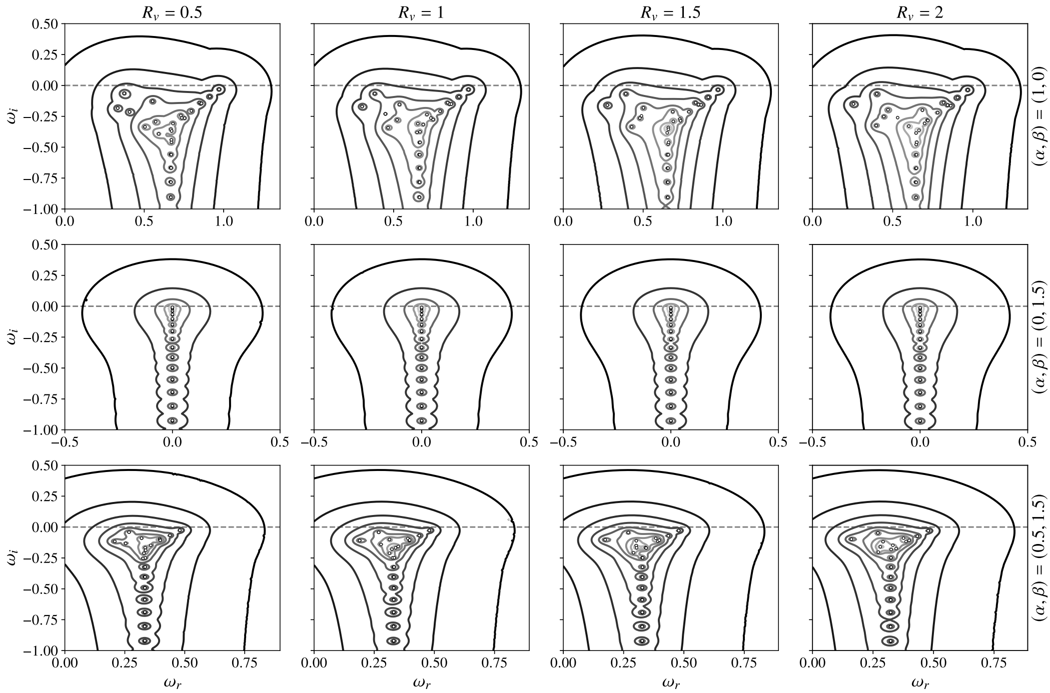

FIG. 8. Pseudospectral contours, log $\|\mathsf{R}^{-1}\|_{-E}$, calculated at $R_v = 0.5, 1, 1.5, 2$ (left-to-right) for some representative wave number pairs. Darker to lighter (or, alternatively, outer to inner) shades correspond to decreasing contour values, i.e., increasing amplification. Top row, $(\alpha, \beta) = (1, 0)$, with contours in each panel ranging from -0.5 to -4 in decrements of -0.5; middle row, $(\alpha, \beta) = (0, 1.5)$, with contours ranging from -0.6 to -3 in decrements of -0.6; and bottom row, $(\alpha, \beta) = (0.5, 1.5)$, with contours ranging from -0.5 to -4.5 in decrements of -0.5. The associated spectra (in terms of ω) have been denoted by circles.

$\mathcal{R} \approx 1000$ at $R_v = 0$). This is the first indication of the unreliability of eigenvalues; when the effects of nonnormality are taken into account, weak crossflows are, in fact, the most prone to excitation.

Interestingly, for relatively large R_v, Fig. 7(a) indicates that $\mathcal{R}$ tends to decay for longitudinal perturbations; in contrast, an increasingly stronger response from spanwise-independent modes is seen in Fig. 7(b), a gap that appears to peak at $R_v \approx 40$. More generally, in intermediate R_v regimes, oblique disturbances constitute the main preference, as highlighted through the level sets of $\mathcal{R}$ in the (α, β) plane in Fig. 7(c). Compared to the crossflow-independent case, these trends are inherently distinct but not unexpected, since the addition of a third-order inertial term in the Orr-Sommerfeld-Squire system fundamentally alters its anatomy and, therefore, that of the underlying nonnormality (see the Appendix). However, what is crucial to note here is that $\mathcal{R}$ is only truly attenuated when R_v becomes very large, say $R_v \geqslant 70$. In other words, it is, in fact, the weakest crossflows that instigate the strongest linear growth, possibly transition arising from subsequent nonlinear processes. Given that most practical applications are typically noise-heavy and that such (relatively) strong crossflows are often not even feasible, we begin to see that crossflow-based modulation in channels might not be as appropriate a choice as suggested in the previous literature.

Moving to the complex plane, $\upsilon \in \mathbb{C}$, in Fig. 8, we illustrate, as is customary, the contours of $\|\mathsf{R}^{-1}\|_{-E}$, where

$$\|\mathsf{R}^{-1}\|_{-E} = \sigma_{\min}(\mathsf{Q}\mathsf{R}^{-1}\mathsf{Q}^{-1}) \tag{39}$$

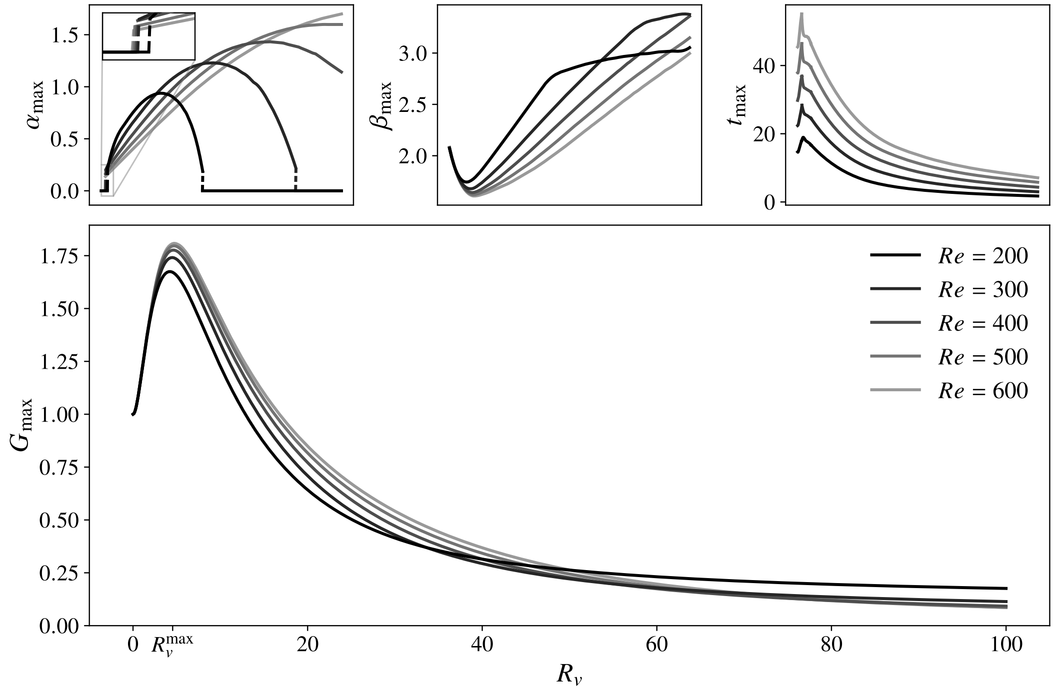

FIG. 9. Plots of $G_{\max}$ versus R_v, normalized against $G_{\max}(\mathrm{Re}, R_v = 0)$, for Re = 200 to Re = 600 in increments of 100. $R_v = R_v^{\max}$, marked appropriately, denotes the crossflow strength that suffers the largest algebraic growth. Top: the wave numbers ($\alpha_{\max}, \beta_{\max}$) and the time $t = t_{\max}$ corresponding to $G_{\max}$.

and $\sigma_{\min}$ represents the minimum singular value of the operator $\mathsf{Q}\mathsf{R}^{-1}\mathsf{Q}^{-1}$. To interpret this in the context of the ϵ-pseudospectra, we note that $\|\mathsf{R}\|_E = \|\mathsf{R}^{-1}\|_{-E}^{-1}$, so that

$$\Lambda_\epsilon = \{\upsilon \in \mathbb{C} : \|\mathsf{R}^{-1}\|_{-E} \leqslant \epsilon\}. \tag{40}$$

Thus, within the level set $\|\mathsf{R}^{-1}\|_{-E} = \epsilon$, amplification of the order of $1/\epsilon$ can be induced as a consequence of harmonic forcing. The pseudospectra are extremely informative, revealing crucial insight on the sensitivity of the spectrum to operator-level perturbations (see [36,37]) or, as is more relevant here, energy growth in the unforced initial-value problem [26]. In particular, substantial transient growth can be achieved if the pseudospectra protrude significantly into the unstable half-plane, a behavior immediately observable in Fig. 8 for all wave number combinations presented. Additionally, strong pseudo-resonance down to $\epsilon \approx 10^{-5}$ is computed, indicative yet again of the underlying nonnormality pervading the linear dynamics of this system. Reminiscent of the trends shown in Fig. 7, this amplification evidently worsens in tandem with the crossflow strength, eventually decaying only in the intermediate to large R_v range (which is not shown here).

We now turn to the unforced problem. In particular, for various Re, Fig. 9 summarizes a numerical sweep for $G_{\max}$, defined as the maximum admissible transient gain in energy over time and across wave number space, i.e.,

$$G_{\max}(\mathrm{Re}, R_v) = \max_{\alpha,\beta,t} G(\alpha, \beta, \mathrm{Re}, R_v, t). \tag{41}$$

Here, to concentrate specifically on amplification that occurs in the absence of exponential instability, we have limited our analysis to Reynolds numbers that are globally subcritical, Re $\lessapprox$ 650. In doing so, we readily observe a familiar pattern: for all Re considered here, peak energy growth is only enhanced by small levels of crossflow, with $R_v = R_v^{\max} \approx 4.5$ consistently characterizing

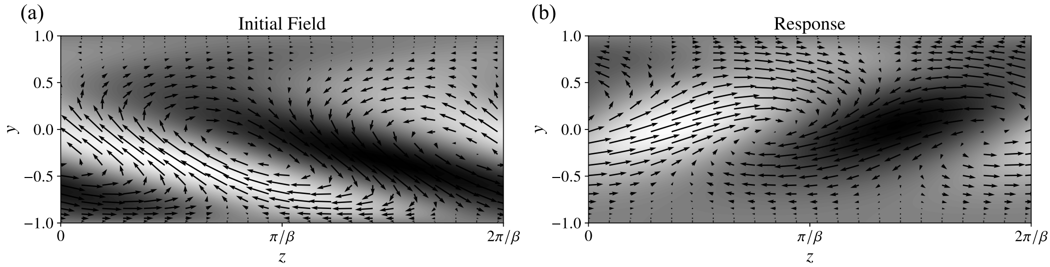

FIG. 10. Cross-stream (y–z) view of (a) the initial perturbation and (b) the response at optimal time associated with $G_{\max}$ for $R_v = R_v^{\max}$. Color and arrows represent, respectively, the streamwise and cross-stream components.

the worst-case scenario. Furthermore, it is precisely at very large R_v that $G_{\max}$ begins to appreciably weaken relative to the Poiseuille flow. Note that for the asymptotic suction boundary layer, Ref. [18] reported a similarly declining—but still significant—amplification relative to the Blasius (no suction) case, although this conclusion could very well be specific to the Reynolds number they opted to focus on.

Regardless, we note that for small R_v (say, $R_v \leqslant 2$), the optimal gain is achieved for streamwise-elongated perturbations, after which oblique modes become the norm (note that Ref. [17] apparently did not see the former for Re $= 1000$). Interestingly, however, at the lower end of the Reynolds numbers treated here, sufficiently strong crossflows can once again establish a preference for streamwise-independent disturbances; we conjecture that expanding the range of R_v investigated might lead to similar behavior at larger Re, although we did not attempt to verify this. Finally, the optimal time $t_{\max}$ also temporarily increases and then decreases monotonically in conjunction with R_v (equivalently $G_{\max}$), although its peak was found instead at $R_v \approx 2 \neq R_v^{\max}$. The immediate implication is that algebraic growth operates on much longer timescales in the presence of crossflow. Reference [18] concluded similarly for ASBL but the effect is, in a sense, more pronounced here, since $G_{\max}$ also increases.

Figure 10 shows the initial condition and response pair attached to the optimal gain calculated for $R_v = R_v^{\max}$. Streaky structures, supported in both x and z, develop at initial time and are then subsequently tilted and advected toward the suction boundary. A crucial question here is the precise mechanism driving the variation in the disturbance energy. It is well-known that longitudinal perturbations develop primarily via the lift-up effect, whereby strong streamwise streaks develop as a consequence of mean momentum transport in the wall-normal direction [38–40]. However, for perturbations with finite streamwise wave numbers, the tilting mechanism of Orr dominates instead [41,42]. In oblique disturbances, these processes operate simultaneously and Ref. [17] argued using a decomposition of the energy production proposed by Ref. [43] that at larger R_v, the Orr mechanism became increasingly relevant. When juxtaposed with Fig. 9, this result should not be too surprising, since $\alpha_{\max}$ generally also increases with R_v. To refine this approach, however, we consider the time variation of the perturbation energy contained in each velocity component [44],

$$\frac{d\mathsf{E}_u}{dt} \equiv \frac{d}{dt}\int_{-1}^{1}\frac{uu}{2}\,dy = \int_{-1}^{1}\underbrace{-uv\frac{\partial U}{\partial y}}_{\mathsf{PR}_u}\,dy + \int_{-1}^{1}\underbrace{-u\frac{\partial p}{\partial x}}_{\mathsf{PVC}_u}\,dy + \int_{-1}^{1}\underbrace{\frac{1}{\mathrm{Re}}u\frac{\partial^2 u}{\partial x_i\partial x_i}}_{\mathsf{VD}_u}\,dy, \tag{42}$$

$$\frac{d\mathsf{E}_v}{dt} \equiv \frac{d}{dt}\int_{-1}^{1}\frac{vv}{2}\,dy = \int_{-1}^{1}\underbrace{-v\frac{\partial p}{\partial y}}_{\mathsf{PVC}_v}\,dy + \int_{-1}^{1}\underbrace{\frac{1}{\mathrm{Re}}v\frac{\partial^2 v}{\partial x_i\partial x_i}}_{\mathsf{VD}_v}\,dy, \tag{43}$$

$$\frac{d\mathsf{E}_w}{dt} \equiv \frac{d}{dt}\int_{-1}^{1}\frac{ww}{2}\,dy = \int_{-1}^{1}\underbrace{-w\frac{\partial p}{\partial z}}_{\mathsf{PVC}_w}\,dy + \int_{-1}^{1}\underbrace{\frac{1}{\mathrm{Re}}w\frac{\partial^2 w}{\partial x_i\partial x_i}}_{\mathsf{VD}_w}\,dy, \tag{44}$$

where PR_j represents energy production, PVC_j the pressure-velocity correlation, and VD_j the viscous dissipation. The term(s) PVC_j can be further decomposed as follows:

$$\mathsf{PVC}_j = u_j \frac{\partial p}{\partial x_j} = -p\frac{\partial u_j}{\partial x_j} + \frac{\partial (u_j p)}{\partial x_j} \equiv \mathsf{PS}_j + \mathsf{PD}_j, \tag{45}$$

where a repeated index does not imply summation. In Eq. (45), PS_j represents the pressure rate-of-strain and PD_j the so-called pressure diffusion.

From here, we note that when $\alpha = 0$, PVC_u vanishes, so that E_v and E_w decay simply due to a combination of the intervariance pressure redistribution and viscous dissipation. As a result, we have $\mathsf{E} \approx \mathsf{E}_u$, whose growth in turn depends on the injection of energy from the mean shear through PR_u. In other words, any changes in the amplification of streamwise-independent modes can be primarily attributed to modifications in the base shear and, by extension, to the Reynolds stresses. However, when $\beta = 0$, the off-diagonal term in the Orr-Sommerfeld-Squire operator vanishes, so that the impact of nonnormality is anyway diminished. Thus, we are left to deal primarily with oblique disturbances. In what follows, the pressure diffusion term PD_j was found to contribute negligibly to PVC_j and has therefore been omitted for the sake of clarity.

Using the energy-optimal initial conditions associated with $R_v = R_v^{\max}$ and $R_v = 20$ (note that these disturbances are both oblique), Fig. 11 compares the development of the energy budget over time for each component of the velocity. The primary motivator for the discrepancy in $G_{\max}$ can be immediately identified as the significantly attenuated production term, which evidently tapers around $t = 45$ for $R_v = 20$. In contrast, PR_u for $R_v = R_v^{\max}$ operates longer and achieves much larger amplitudes. Furthermore, pressure redistribution remains active in both cases, although its influence is much more pronounced for the suboptimal $R_v = 20$. On inspection, this energy is transferred to both the wall-normal and the spanwise perturbations, and it is interesting to note that E_v ultimately achieves a slightly larger amplitude for $R_v = 20$, so that a stronger amplification of the streaks observed in Fig. 10 might be expected due to the lift-up process. However, we see that this effect is negated not only by a moderate increase in dissipation, but also by the rapid extraction of energy from E_v to E_w through a strongly negative pressure redistribution term starting from, say, $t \approx 12.5$. Consequently, any increase in the wall-normal perturbations is quickly eroded and energy production suffers. The net influx of energy into E_w appears to primarily dissipate away, in part, due to the lack of a feedback mechanism (e.g., a mean spanwise shear) to amplify it.

V. THE PRESENCE OF WALL VELOCITY

If either wall is translated in the streamwise direction with some finite velocity, say $U_c \neq 0$, then we recover the base flow of Refs. [3,6]. More specifically, if this moving boundary is taken to be the upper (suction) one, then the dimensionless streamwise velocity becomes

$$U(y, \xi, R_v) = \begin{cases} R_v(\xi R_v + 4y + (4 - \xi R_v)\coth R_v - e^{R_v y}(4 - \xi R_v)\operatorname{csch} R_v)/\big(\xi R_v^2 - 4 + \Xi_1\big), & \xi R_v \leqslant \Xi_2, \\ \big(\xi R_v + 4y + (4 - \xi R_v)\coth R_v - e^{R_v y}(4 - \xi R_v)\operatorname{csch} R_v\big)/2\xi R_v, & \xi R_v > \Xi_2, \end{cases} \tag{46}$$

where $\xi = U_c/U_p$ and we have adopted a nondimensionalization similar to that in Sec. II A. Furthermore, we have denoted

$$\Xi_1 = R_v(4 - \xi R_v)\coth R_v - 4\log\left(R_v(4 - \xi R_v)\operatorname{csch} R_v/4\right), \tag{47}$$

$$\Xi_2 = 4(1 - \sinh R_v/R_v e^{R_v}). \tag{48}$$

We note two distinct scenarios in Eq. (46), the need for which arises from the fact that both the crossflow and the Couette component skew the velocity profile toward the upper half of the

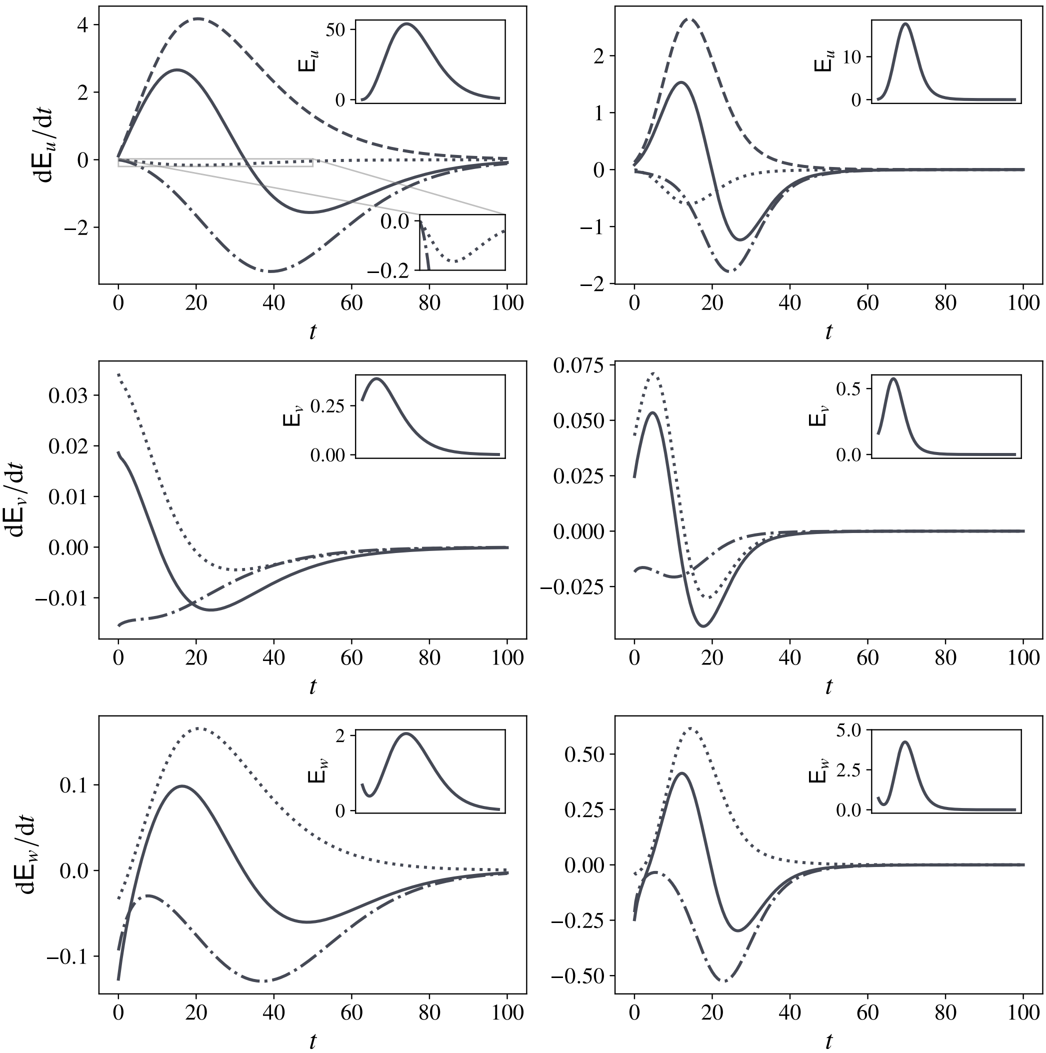

FIG. 11. Budgets for the perturbation energy contained in each velocity component; left column, $R_v = R_v^{\max}$ and right column, $R_v = 20$. In each panel, a dashed line indicates energy production, dotted, pressure redistribution, dash-dot, viscous dissipation, and solid, total. The insets show the variation of the perturbation energies E_u, E_v, and E_w in time.

channel [6]. Thus, for strong enough crossflows (alternatively, large enough wall speeds), the maximum of the streamwise velocity will necessarily occur at the moving boundary, that is, $U_m = U_c$ and $y(U = U_m) = h$. If the pair (ξ, R_v) is chosen such that $\xi R_v = 4 > \Xi_2$, then one recovers $U(y, \xi, R_v) = y$, which constitutes the "generalized" Couette profile of Ref. [9]. Throughout this section, we limit our attention to wall speeds $\xi \in [0, 1]$, as in the prior literature.

A. Modal instability between $20.8 \leqslant R_v \leqslant 22$ for $\xi > 0$

Although not the primary focus in this work, we begin by reporting in Table I samples from a set of novel instabilities that we were able to compute for Couette-Poiseuille flow with crossflow for $20.8 \leqslant R_v \leqslant 22$. Previous work in this range by Ref. [6] posited unconditional linear *stability*

TABLE I. Flow parameters at criticality for select pairs (ξ, R_v) such that $20.8 \leqslant R_v \leqslant 22$; N_{conv} represents the resolution (number of Chebyshev modes) that was required for resolving the instability (i.e., that the instability remained robust to further increases in numerical fidelity).

R_v	ξ	Re_c ($\times 10^6$)	α_c	N_{conv}
21.9	0.015	1.083334	3.956539	512
20.9	0.025	1.080632	3.956539	512
21.75	0.03	1.175339	4.144285	512
21	0.05	1.272604	4.037017	512
21.25	0.075	1.569059	4.340941	512
21.5	0.1	2.043112	4.546928	512
21.55	0.125	2.859688	5.225415	1024
21.3	0.16	6.950775	8.307361	2560

for all $\xi \geqslant 0$. However, as demonstrated in Sec. III and as is now apparent here, this is clearly an inaccurate conclusion that arises again from a combination of a lack of polynomial resolution and a truncated search region. Despite this, we determined that the instability was short-wavelength, roughly consistent with the trends they calculated as $R_v \to 20.8$ (cf. Fig. 20 in their paper). Although we did not conduct a detailed investigation to verify this, our numerical experiments suggest that the bounds offered in the stability phase diagram of Ref. [6] might not be robust and could potentially be tightened if spatial discretization is refined.

B. Transient growth

For various choices of the nondimensional wall speed ξ, Fig. 12(a) illustrates how the optimal gain $G_{\max}$ is modified in the presence of both crossflow and wall motion at $\text{Re} = 500$ (which remains globally subcritical for $\xi > 0$). Two main regions of development can be identified, related, respectively, to the two cases defined in Eq. (46). In particular, when $\xi R_v \leqslant \Xi_2$, the effect of wall motion is evidently minor, because while the maximum energy growth generally increases, it does so only to remain around the same order as $G_{\max}$ for simple Poiseuille flow with crossflow (that is, without wall motion). The most noticeable change occurs in a short range around $R_v = R_v^{\max}$,

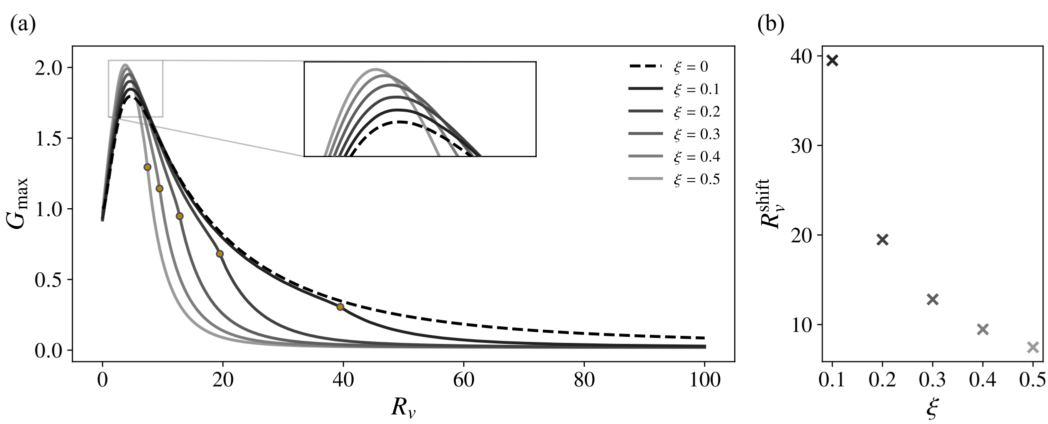

FIG. 12. (a) Plots of $G_{\max}$, the maximal energy gain, in the presence of wall motion versus R_v for $\xi > 0$ and $\text{Re} = 500$; the reference case, $\xi = 0$, is depicted with a dashed line. All curves have been normalized by $G_{\max}$ at this Re for Poiseuille flow, $\xi = 0 = R_v$. The yellow circles depict the minimal crossflow Reynolds number R_v^{shift} such that $\xi R_v > \Xi_2$, cf. Eq. (46); these have been separately visualized in panel (b).

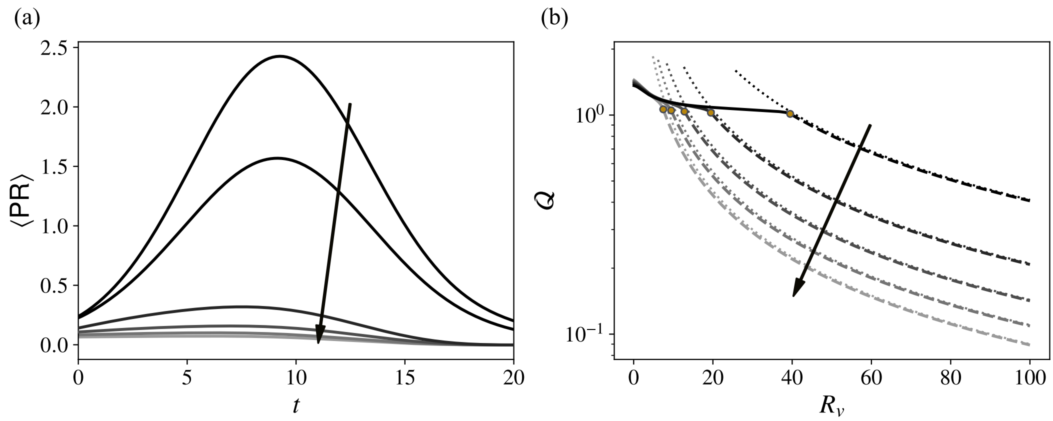

FIG. 13. (a) For the initial condition associated with $G_{\max}$, the evolution of the energy production in time at $R_v = 45$ for the ξ treated in Fig. 12(a) (note that $\xi R_v > 4$ is always satisfied for this choice of the crossflow). (b) Flow rate $\mathcal{Q}$; for each wall speed, the value R_v^{shift} is marked with a circle, whereas the dashed lines correspond to the regime $\xi R_v > \Xi_2$. The asymptotic result derived in Eq. (49) is also illustrated (dotted lines). In each panel, ξ increases in the direction of the arrow.

which is highlighted in the inset, although the details here are ultimately immaterial. Despite the substantial increase in Re_c afforded by small R_v coupled with modest wall speeds deemed by Ref. [6] as the most relevant parameters for control purposes, nonmodal mechanisms nevertheless remain significant and are sometimes even amplified. Of course, the situation can only worsen as Re increases.

Theoretically, one could then look toward flow parameters such that $\xi R_v > \Xi_2$ [Fig. 12(b) plots $R_v = R_v^{\text{shift}}$ initiating this regime] and, indeed, Fig. 12(a) indicates that for sufficiently large wall speeds, successively weaker crossflows can considerably suppress algebraic growth. At first glance, this is encouraging, but it is not without its own caveats. Specifically, an increase in R_v (or ξ) for this regime is equivalent to a decrease in the background shear $\mathsf{D}U$, which asymptotically behaves as $\mathsf{D}U \sim 2/(\xi R_v)$. Consequently, as we highlight in Fig. 13(a), the energy production must also decrease. However, what is alarming is that, in this limit, the flow itself is, in fact, being killed off. To verify this, it is easiest to consider the nondimensional volumetric flow rate $\mathcal{Q}$ which, for $\xi R_v > \Xi_2$, behaves as

$$\mathcal{Q} \sim \frac{1}{R_v} + \frac{4}{\xi R_v}, \tag{49}$$

so that counterproductively, $\mathcal{Q} \to 0$ at large R_v; see Fig. 13(b).

VI. DISCUSSION AND CONCLUSION

We have performed a detailed reassessment of stability in channel flows with crossflow. Previous work has attempted to determine parameter regimes supposedly ideal for delaying transition, and our primary contribution in this work has been to show that nonmodal growth may preclude this apparent suitability.

The main focus of our study has been the Poiseuille flow in the presence of crossflow. Beginning with an eigenvalue (modal) analysis, we provide a global perspective on modal instability by tracking the trajectory of the neutral stability curves in the (α, Re) space. We show that beyond a discontinuity in the critical parameters, two individual neutral curves begin to coexist, with distinct properties exemplified through consideration of the corresponding linear energetics. The movement of the critical layers is shown to be highly relevant in shaping the development of this budget.

From a nonmodal perspective, which forms the crux of this paper, the resolvent is first inspected for real frequencies, and later the more general complex case through the ϵ-pseudospectra. Substantial amplification is recovered even at relatively mild subcritical Re, and is only damped for large, possibly unfeasible, crossflows. Similar patterns are observed when treating unforced algebraic growth, with nonmodal interactions lasting longer (relative to the reference Poiseuille flow) and being more dangerous at weak R_v—touted in the previous literature as the "ideal" stability configuration. The precise mechanism driving (and suppressing) energy growth is explored by considering a componentwise energy budget. The additional stability provided by large R_v is shown to be due to a combination of decreased energy production and a more active velocity-pressure gradient term, which forces intercomponent redistribution of energy in a way that significantly dampens the wall-normal fluctuations and, therefore, the lift-up effect.

This analysis has been extended to account for wall motion, cf. the flow of Ref. [6]. Here, we present novel instabilities for a region of parameter space previously thought to be unconditionally linearly stable. These instabilities occur at very high Re but are physically genuine and of the short-wavelength type. Optimal growth is found to only worsen with the inclusion of wall motion, except beyond a regime change in the parameter space defined by $R_v = R_v^{\text{shift}}(\xi)$, where the background shear decays as $1/(\xi R_v)$ in the channel bulk. Here, the decrease in energy production is nonetheless counter-productive, since it is shown to be accompanied by an impractical cessation of mass transport brought on by a skewing of the velocity profile due to the combined effect of crossflow and wall motion. Collectively, our results suggest that crossflow-based stabilization schemes, at least in internal flows, are unlikely to be effective.

ACKNOWLEDGMENTS

This research was supported financially by G.P's startup grant through the University of Pennsylvania. M.A. thanks Professor Jeffrey Oishi for helpful comments that improved the clarity of the material presented here. Computing resources were provided by the University of Pennsylvania (Chestnut cluster) and the Bates College Leavitt Cluster.

APPENDIX: EFFECT OF THE MEAN WALL-NORMAL VELOCITY

An intriguing assertion put forward by Ref. [18] for the asymptotic suction boundary layer was that the reduction in G relative to the reference Blasius case was primarily a consequence of variations in the streamwise velocity profile and not due to the auxiliary terms introduced in the Orr-Sommerfeld-Squire system by the nonzero mean wall-normal velocity. In contrast, Ref. [6] determined that the influence of these auxiliary terms on the spectra was, in fact, relevant, although only when R_v was large. In a similar manner, here, we wish to categorize the impact of crossflow on algebraic growth between its two main contributions, that is, the inertial operator $\mathcal{I}$,

$$\mathcal{I} \equiv V \frac{\partial}{\partial y} \nabla^2, \tag{A1}$$

cf. Eqs. (10) and (11) and the asymmetry imposed on the streamwise velocity profile U. We follow the previous approaches. In particular, for some sample wave number pairs, Fig. 14 plots the gain G as a function of time for $R_v = 1$, $R_v = 15$, and the Poiseuille flow ($R_v = 0$). For $R_v \neq 0$, two sets of stability equations are considered, one with and the other without the operator $\mathcal{I}$, although both retain the U derived in the presence of crossflow. Therefore, the latter case is equivalent to setting $V = 0$ *a posteriori*. Interesting phenomena are observed; specifically, in all cases, including the crossflow term *dampens* the energy gain relative to when it is excluded. However, in line with the findings of Ref. [6], this disparity only becomes significant for $R_v = 15$. In particular, for the latter, it is apparent that the crossflow-affected U by itself can generate a much stronger response for streamwise-independent disturbances compared to not only the Poiseuille flow but also the equivalent profile at $R_v = 1$ (which, as suggested in Fig. 9 should, in fact, be the more "dangerous"

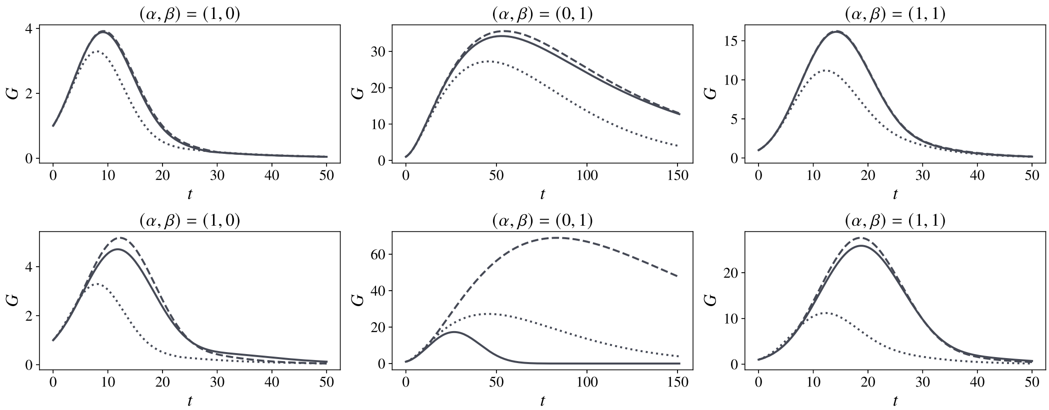

FIG. 14. Gain G plotted against time for $R_v = 1$ (top) and $R_v = 15$ (bottom) for (left to right), $(\alpha, \beta) = (1, 0)$, $(\alpha, \beta) = (0, 1)$, and $(\alpha, \beta) = (1, 1)$. Solid lines indicate calculations with the crossflow term and dashed lines without. The dotted line in each panel represents Poiseuille flow.

scenario). This potential for growth is, of course, significantly suppressed when the inertial operator is taken into account.

Thus, we conclude that the crossflow has a dual impact on nonmodal stability. At small R_v, its influence is felt predominantly through changes in the background streamwise flow (hence the negligible differences observed in Fig. 14). However, for large R_v, the third-order differential term in Eq. (A1) is of greater relevance, likely impacting energy amplification directly through variations in the perturbations themselves (and, by extension, the energy budget; see the discussion toward the end of Sec. IV).

[1] R. D. Joslin, Aircraft laminar flow control, Annu. Rev. Fluid Mech. **30**, 1 (1998).

[2] K. Krishnan, O. Bertram, and O. Seibel, Review of hybrid laminar flow control systems, Prog. Aerosp. Sci. **93**, 24 (2017).

[3] F. D. Hains, Stability of plane Couette–Poiseuille flow with uniform crossflow, Phys. Fluids **14**, 1620 (1971).

[4] D. M. Sheppard, Hydrodynamic stability of the flow between parallel porous walls, Phys. Fluids **15**, 241 (1972).

[5] J. H. M. Fransson and P. H. Alfredsson, On the hydrodynamic stability of channel flow with cross flow, Phys. Fluids **15**, 436 (2003).

[6] A. Guha and I. A. Frigaard, On the stability of plane Couette–Poiseuille flow with uniform crossflow, J. Fluid Mech. **656**, 417 (2010).

[7] M. C. Potter, Stability of plane Couette–Poiseuille flow, J. Fluid Mech. **24**, 609 (1966).

[8] V. A. Romanov, Stability of plane-parallel Couette flow, Funct. Anal. Appl. **7**, 137 (1973).

[9] F. Nicoud and J. R. Angilella, Effects of uniform injection at the wall on the stability of Couette-like flows, Phys. Rev. E **56**, 3000 (1997).

[10] R. R. Kerswell, Instability driven by boundary inflow across shear: A way to circumvent Rayleigh's stability criterion in accretion disks? J. Fluid Mech. **784**, 619 (2015).

[11] M. B. Zaturska, P. G. Drazin, and W. H. H. Banks, On the flow of a viscous fluid driven along a channel by suction at porous walls, Fluid Dyn. Res. **4**, 151 (1988).

[12] E. B. B. Watson, W. H. H. Banks, M. B. Zaturska, and P. G. Drazin, On transition to chaos in two-dimensional channel flow symmetrically driven by accelerating walls, J. Fluid Mech. **212**, 451 (1990).

[13] L. N. Trefethen, A. E. Trefethen, S. C. Reddy, and T. A. Driscoll, Hydrodynamic stability without eigenvalues, Science **261**, 578 (1993).

[14] L. N. Trefethen and M. Embree, *Spectra and Pseudospectra: The Behavior of Nonnormal Matrices and Operators* (Princeton University Press, Princeton, NJ, 2005).

[15] P. Schmid and D. Henningson, *Stability and Transition in Shear Flows*, Applied Mathematical Sciences (Springer, New York, NY, 2001).

[16] L. Brandt, The lift-up effect: The linear mechanism behind transition and turbulence in shear flows, Eur. J. Mech. B Fluids **47**, 80 (2014).

[17] C. Chen, J.-T. Huang, and W.-G. Zhang, Optimal perturbations in viscous channel flow with crossflow, Fluid Dyn. Res. **53**, 025502 (2021).

[18] J. H. Fransson and P. Corbett, Optimal linear growth in the asymptotic suction boundary layer, Eur. J. Mech. B Fluids **22**, 259 (2003).

[19] T. Kurian and J. Fransson, Transient growth in the asymptotic suction boundary layer, Exp. Fluids **51**, 771 (2011).

[20] S. Cherubini, P. De Palma, and J.-C. Robinet, Non-linear optimal perturbations in the asymptotic suction boundary-layer, Procedia IUTAM **14**, 246 (2015).

[21] P. J. Schmid, Nonmodal stability theory, Annu. Rev. Fluid Mech. **39**, 129 (2007).

[22] K. M. Butler and B. F. Farrell, Three-dimensional optimal perturbations in viscous shear flow, Phys. Fluids **4**, 1637 (1992).

[23] C. Cossu, G. Pujals, and S. Depardon, Optimal transient growth and very large–scale structures in turbulent boundary layers, J. Fluid Mech. **619**, 79 (2009).

[24] C. Cossu and Y. Hwang, Self-sustaining processes at all scales in wall-bounded turbulent shear flows, Philos. Trans. R. Soc. A **375**, 20160088 (2017).

[25] D. Variale, E. Parente, J. C. Robinet, and S. Cherubini, Modal and nonmodal stability analysis of turbulent stratified channel flows, Phys. Rev. Fluids **9**, 013904 (2024).

[26] S. C. Reddy, P. J. Schmid, and D. S. Henningson, Pseudospectra of the Orr-Sommerfeld operator, SIAM J. Appl. Math. **53**, 15 (1993).

[27] L. N. Trefethen, *Spectral Methods in MATLAB* (SIAM, Philadelphia, PA, 2000).

[28] M. Abdullah and G. I. Park, Linear stability analysis of oblique Couette–Poiseuille flows, J. Fluid Mech. **998**, A25 (2024).

[29] P. Moritz, R. Nishihara, S. Wang, A. Tumanov, R. Liaw, E. Liang, M. Elibol, Z. Yang, W. Paul, M. I. Jordan, and I. Stoica, Ray: A distributed framework for emerging AI applications, in *Proceedings of the 13th USENIX Conference on Operating Systems Design and Implementation* (USENIX Association, Carlsbad, CA, 2018), p. 561–577.

[30] J. S. Oishi, K. J. Burns, S. E. Clark, E. H. Anders, B. P. Brown, G. M. Vasil, and D. Lecoanet, Eigentools: A python package for studying differential eigenvalue problems with an emphasis on robustness, J. Open Source Softw. **6**, 3079 (2021).

[31] H. B. Squire, On the stability for three-dimensional disturbances of viscous fluid flow between parallel walls, Proc. R. Soc. London, Ser. A **142**, 621 (1933).

[32] C. C. Lin, On the stability of two-dimensional parallel flows. III. Stability in a viscous fluid, Q. Appl. Math. **3**, 277 (1946).

[33] S. J. Cowley and F. T. Smith, On the stability of Poiseuille-Couette flow: A bifurcation from infinity, J. Fluid Mech. **156**, 83 (1985).

[34] L. M. Mack, Boundary-layer linear stability theory, Tech. Rep. 709, Part 3. AGARD (1984).

[35] B. J. McKeon and A. S. Sharma, A critical-layer framework for turbulent pipe flow, J. Fluid Mech. **658**, 336 (2010).

[36] L. N. Trefethen and D. Bau, *Numerical Linear Algebra* (SIAM, Philadelphia, PA, 1997).

[37] S. Symon, K. Rosenberg, S. T. M. Dawson, and B. J. McKeon, Non-normality and classification of amplification mechanisms in stability and resolvent analysis, Phys. Rev. Fluids **3**, 053902 (2018).

[38] T. Ellingsen and E. Palm, Stability of linear flow, Phys. Fluids **18**, 487 (1975).

[39] M. T. Landahl, Wave breakdown and turbulence, SIAM J. Appl. Math. **28**, 735 (1975).

[40] M. T. Landahl, A note on an algebraic instability of inviscid parallel shear flows, J. Fluid Mech. **98**, 243 (1980).

[41] W. M. Orr, The stability or instability of the steady motions of a perfect liquid and of a viscous liquid. Part II: A viscous liquid, Proc. Roy. Irish Acad. Sec. A: Math. Phys. Sci. **27**, 69 (1907).

[42] Y. Jiao, Y. Hwang, and S. I. Chernyshenko, Orr mechanism in transition of parallel shear flow, Phys. Rev. Fluids **6**, 023902 (2021).

[43] B. F. Farrell and P. J. Ioannou, Optimal excitation of three-dimensional perturbations in viscous constant shear flow, Phys. Fluids **5**, 1390 (1993).

[44] M. J. P. Hack and T. A. Zaki, Modal and non-modal stability of boundary layers forced by spanwise wall oscillations, J. Fluid Mech. **778**, 389 (2015).